Journal of Advanced Ceramics
先进陶瓷
ISSN 2226-4108
CN 10-1154/TQ
清华大学出版社 Tsinghua University Press
SciOpen

J Adv Ceram 2026, **15**: 9221403
https://doi.org/10.26599/JAC.2026.9221403
Research Article

Electronic-instability-driven phase separation enables grain-boundary toughening in high-entropy carbides

Yimin Ouyang[1,†], Saidi Wang[1,†], Wenqi Zhu[1], Jincheng Wu[1], Tao Zhang[1], Mengdong Ma[2,3,*], Bin Du[1,*]

[1]*School of Physics and Materials Science, Guangzhou University, Guangzhou 510006, China*

[2]*Center for High Pressure Science (CHiPS), State Key Laboratory of Metastable Materials Science and Technology, Yanshan University, Qinhuangdao, Hebei 066004, China*

[3]*State Key Laboratory of Crane Technology, Yanshan University, Qinhuangdao 066004, China*

†These authors are equally for this work.

*Corresponding author:

E-mail: M. Ma, mamengdong@ysu.edu.cn;

B. Du, dubin@gzhu.edu.cn;

Received: June 22, 2026; Revised: November 3, 2026; Accepted: November 4, 2026
©The Author(s) 2026

Just Accepted

Abstract

High-entropy carbides (HECs) can exhibit enhanced phase stability, although elemental segregation and phase separation may occur under certain conditions. However, how intrinsic phase instability evolves under high pressure and how it can be exploited to regulate mechanical properties remain insufficiently understood. Here, $(Hf_{(1-X)/4}Zr_{(1-X)/4}Nb_{(1-X)/4}Ta_{(1-X)/4}Co_X)C$ (X = 0.14, 0.18, and 0.20) was investigated by integrating first-principles calculations with high-pressure sintering. The decomposition Gibbs free energy remains negative from 0 to 6 GPa, indicating an intrinsic thermodynamic driving force for Co segregation. Electronic-structure analysis reveals that pressure amplifies the bonding asymmetry between the stable transition-metal–C framework and the comparatively weaker Co–C interactions, as evidenced by the opposite pressure-dependence change in their integrated crystal orbital Hamiltonian population values. This bonding asymmetry is accompanied by local structural rearrangement, with the first Co–Co radial distribution function (RDF) peak shifting from 3.14 to 3.10 Å and increasing in intensity from 15.97 to 24.50. Experimentally, Co segregates into a ductile FCC phase preferentially distributed along grain boundaries, accompanied by an increase in the low-angle grain boundary fraction from 20.2% to 37.9%, indicating a possible contribution to local strain accommodation. The resulting heterogeneous microstructure facilitates crack deflection and branching, leading to an increase in fracture toughness from 4.5 ± 0.2 to 5.0 ± 0.2 $MPa \cdot m^{1/2}$. These

Just Accepted

findings demonstrate that pressure-driven electronic instability can be exploited to transform intrinsic phase instability into beneficial microstructural heterogeneity, providing a new strategy for toughening high-entropy ceramics.

Keywords: High-entropy carbide; High-pressure sintering; First-principles calculations; Mechanical Properties; Toughening

Just Accepted

1. Introduction

High-entropy carbides (HECs) [1–3] have attracted extensive attention owing to their exceptional combination of hardness, thermal stability, oxidation resistance, and chemical inertness. These attractive properties are commonly attributed, in part, to the high-entropy effect, which is generally believed to promote the formation and stabilization of single-phase solid solutions through the contribution of configurational entropy [1,4–6]. Consequently, achieving and maintaining a homogeneous solid-solution state has long been regarded as a fundamental design principle for HECs [7–9]. However, increasing experimental and theoretical evidence suggests that such stabilization is not universal [10–13]. Chemical short-range order, elemental segregation, phase separation, and second-phase precipitation have been observed in compositionally complex carbides, particularly under non-equilibrium processing conditions or external thermodynamic fields [14–16]. These observations suggest that the high-entropy effect alone is insufficient to completely suppress phase separation and that the stability of HEC solid solutions is governed by a delicate competition among configurational entropy, local bonding characteristics, lattice distortion, and thermodynamic driving forces. Therefore, understanding the stability limits of high-entropy solid solutions and the underlying mechanisms governing their phase evolution remains an important issue in the science and design of high-entropy ceramics.

From a mechanical perspective, most single-phase HECs exhibit excellent hardness but relatively limited fracture toughness, which remains a major obstacle for their structural application [17,18]. Considerable efforts have therefore been devoted to

Just Accepted

introducing heterogeneous microstructures to improve crack resistance [19–23]. Existing strategies mainly rely on externally introduced reinforcements, including particle additions [24], fiber [25], nanocomposite design [26], carbon nanotubes [27], graphene [28], and gradient structure [29]. Although these approaches can effectively enhance toughness, they often suffer from complicated processing routes, limited interfacial controllability, and difficulties in achieving homogeneous phase distribution. In contrast, phase separation originating from intrinsic thermodynamic instability may provide an alternative pathway for microstructural engineering. Rather than being regarded solely as a detrimental phenomenon, controlled phase instability could enable the in-situ formation of secondary phases and heterointerfaces capable of accommodating deformation and dissipating fracture energy. Such a strategy would allow toughening to be achieved without sacrificing the intrinsic advantages of the high-entropy matrix. Nevertheless, current studies have primarily focused on the structural consequences of precipitated phases, whereas the thermodynamic origin of phase separation, its electronic-structure basis, and its potential role in toughening remain largely unexplored. As a result, the possibility of transforming phase instability from a degradation mechanism into a controllable toughening strategy has rarely been explored.

Among the available thermodynamic variables, pressure represents a particularly powerful yet largely unexplored parameter for regulating phase stability in HECs [30–32]. Unlike temperature, which mainly influences configurational entropy, pressure directly modifies the Gibbs free energy through the PΔV term and therefore can

Just Accepted

fundamentally alter the thermodynamic stability landscape of compositionally complex ceramics [33]. In addition, pressure affects atomic packing efficiency [34], local bonding environments, and lattice distortion, potentially triggering conditions [35]. Despite these unique effects, the role of pressure in governing phase separation in HECs remains poorly understood. Among transition metals, Co provides an ideal model system for investigating pressure-induced phase instability. Unlike refractory carbide-forming elements such as Hf, Zr, Nb, and Ta, Co exhibits weak carbide-forming ability and distinct electronic characteristics [36–40]. Consequently, Co is expected to occupy a metastable state within the carbide lattice and may become particularly sensitive to external thermodynamic perturbations. Although Co segregation has occasionally been observed in Co-containing HECs, the underlying thermodynamic origin, the electronic structure mechanism responsible for destabilization, and the influence of pressure on these processes remain unclear. More importantly, it remains unknown whether pressure-induced phase separation can be deliberately exploited to create beneficial heterointerfaces and thereby improve fracture resistance.

In this study, Co-containing HECs, i.e., $(Hf_{(1-X)/4}Zr_{(1-X)/4}Nb_{(1-X)/4}Ta_{(1-X)/4}Co_X)C$ (X = 0.14, 0.18, and 0.20), were selected as a model system to investigate the interplay among pressure, electronic instability, phase separation, and mechanical performance. By combining first-principles calculations, high-pressure sintering, and multiscale structural characterization, we establish a mechanistic framework linking electronic structure, local lattice distortion, and Co clustering behavior. The results reveal that antibonding Co-C interactions generate an intrinsic electronic instability that is

Just Accepted

amplified under pressure, driving Co precipitation through a coupled electronic-structure mechanism. More importantly, the resulting Co-rich interfacial phase promotes strain accommodation and crack-tip shielding, demonstrating that phase instability can be transformed from a traditionally undesirable phenomenon into a viable microstructure design strategy for damage-tolerant high-entropy ceramics.

2. Experimental procedures

2.1 First-principles calculations

First-principles calculations based on density functional theory (DFT) were performed using the Vienna Ab initio Simulation Package (VASP) [41,42]. A 2 × 2 × 2 supercell containing 64 atoms was constructed based on the rock-salt ZrC structure, and special quasi-random structures (SQS) were generated using the Alloy Theory Automated Toolkit (ATAT) to model the chemical disorder of the high-entropy carbide [43]. The generalized gradient approximation (GGA) with the Perdew–Burke–Ernzerhof (PBE) functional was used to describe the exchange-correlation interactions [44]. Projector augmented-wave (PAW) potentials were employed with a plane-wave cutoff energy of 520 eV. The Brillouin zone was sampled using a 4 × 4 × 4 Monkhorst–Pack k-point mesh. The convergence criteria for electronic and ionic relaxations were set to 10^{-6} eV and 0.005 eV·Å^{-1}, respectively. Convergence tests for the k-point mesh are provided in Figure S1 of the Supporting Information.

Structural optimizations were performed under pressures of 0–6 GPa. The density of states (DOS) and crystal orbital Hamilton population (COHP) were analyzed to characterize the electronic structure and chemical bonding, respectively; COHP

Just Accepted

calculations were performed using LOBSTER. The integrated COHP (ICOHP) values were used to evaluate the relative strength of chemical bonding, with more negative values corresponding to stronger bonding interactions. Voronoi and Bader partitioning were used to characterize atomic volumes and local volume misfit, while radial distribution functions (RDFs) were calculated using OVITO to examine pressure-dependent local atomic arrangements and Co–Co correlations. Additional computational details and definitions of the volume-misfit parameters and RDF are provided in the Supporting Information.

2.2 Materials

Tantalum pentachloride ($TaCl_5$, ≥ 98% purity), niobium pentachloride ($NbCl_5$, 99% purity), hafnium tetrachloride ($HfCl_4$, 99.5% purity), zirconium n-propoxide (70 wt.% solution in n-propanol), and cobalt acetylacetonate (98% purity) were used as metal precursors. n-propanol ($CH_3CH_2CH_2OH$, 99% purity) served as the solvent, triethylamine ($C_6H_{15}N$, 98% purity) as the dichlorination reagent, and acetylacetone ($C_5H_8O_2$, 99% purity) as the chelating agent. Phenolic resin (BR purity) served as the carbon source. All chemicals were supplied by Shanghai Maclean Biochemical Technology Co., Ltd. and used without further purification.

2.3 Synthesis of samples

According to our previous work [45], $(Hf_{(1-X)/4}Zr_{(1-X)/4}Nb_{(1-X)/4}Ta_{(1-X)/4}Co_X)C$ (X = 0.14, 0.18, and 0.20) powders were synthesized via the polymer-derived ceramics (PDC) route. Initially, transition-metal chlorides were converted into the corresponding metal alcoholates. The obtained metal alkoxides were mixed in equimolar ratios and

Just Accepted

combined with cobalt acetylacetonate. Subsequently, acetylacetone was added as a complexing agent and stirred for 24 hours. Phenolic resin and deionized water were then introduced, followed by an additional 24 h of stirring. The resulting solution was dried at 200°C to obtain precursor powders. These precursor powders were pyrolyzed at 1900°C for 1 h under an inert atmosphere to obtain high-entropy carbide powders. Bulk ceramics were fabricated using a DS 6×8 MN cubic press (Guilin Guiye Machinery Co., Ltd.) equipped with a graphite heating system. The compositions $(Hf_{0.215}Zr_{0.215}Nb_{0.215}Ta_{0.215}Co_{0.140})C$, $(Hf_{0.205}Zr_{0.205}Nb_{0.205}Ta_{0.205}Co_{0.180})C$, and $(Hf_{0.20}Zr_{0.20}Nb_{0.20}Ta_{0.20}Co_{0.20})C$ were denoted as HEC1, HEC2, and HEC3, respectively. During sintering, the pressure was increased to 6 GPa within 1 min and maintained constant. The samples were heated to 1900°C at a rate of 50 °C/min and held for 5 min under constant pressure. Subsequently, the samples were cooled to room temperature at a rate of 50 °C/min, followed by gradual pressure release at a rate of 0.3 GPa/min.

2.4 Characterization

Phase identification was conducted by X-ray diffraction (XRD) using a Rigaku Ultima IV with Cu Kα radiation (λ = 1.5406 Å), a scanning range of 20°–90°, a step size of 0.02°, and a scanning rate of 5 °/min. Microstructural morphology and elemental distribution were characterized using a JEOL JSM-IT800 scanning electron microscope (SEM) equipped with energy-dispersive spectroscopy (EDS) and electron backscatter diffraction (EBSD). High-resolution microstructural analysis was performed using a FEl Talos F200X transmission electron microscope. The sample was cut from the bulk samples using the focused ion beam (FIB) technique. Nanoindentation tests were

Just Accepted

performed using an Anton Paar NHT2 with loading and unloading rates of 1 mN/s, a maximum load of 20 mN, and a dwell time of 10 s. Vickers hardness was measured using a DHV-1000Z tester under loads ranging from 100 to 1000 g with a dwell time of 15 s. Due to the limited size of high-pressure sintered samples, the fracture toughness (K_{IC}) was estimated using the indentation method [46]:

$$K_{IC} = 0.016\left(\frac{E}{H_V}\right)^{0.5}\left(\frac{P}{c^{1.5}}\right) \quad (1)$$

where H_V is the Vickers hardness, E is the elastic modulus obtained from nanoindentation, P is the applied load, and c is the average crack length measured from the indentation corners. To minimize errors, each sample was tested five times, and the three middle values were selected as the final results.

3. Results and discussion

3.1 Phase and microstructure of the HEC powders

Figure 1 presents the XRD patterns of the $(Hf_{(1-X)/4}Zr_{(1-X)/4}Nb_{(1-X)/4}Ta_{(1-X)/4}Co_X)C$ (X = 0.14, 0.18, and 0.20) powders synthesized via pyrolysis at 1900°C. All diffraction peaks can be indexed to a single face-centered cubic (FCC) phase, without detectable secondary phases within the resolution limits of XRD. The lattice parameters for $(Hf_{0.215}Zr_{0.215}Nb_{0.215}Ta_{0.215}Co_{0.140})C$, $(Hf_{0.205}Zr_{0.205}Nb_{0.205}Ta_{0.205}Co_{0.180})C$, and $(Hf_{0.20}Zr_{0.20}Nb_{0.20}Ta_{0.20}Co_{0.20})C$ are 4.5538 Å, 4.5519 Å, and 4.5517 Å, respectively. This result indicates the formation of a solid-solution high-entropy carbide. A slight peak shift toward higher angles is observed with increasing Co content, indicating lattice contraction induced by Co incorporation. Figure 2 shows the SEM images and corresponding EDS elemental mappings of the HEC powders. As observed in Figures

Just Accepted

2a, c, and e, the powders consist of irregularly shaped particles with noticeable interparticle gaps. Smaller particles are attached to the surfaces of larger ones, indicating a heterogeneous growth behavior during the high-temperature pyrolysis process. The EDS elemental mapping images (Figures 2b, d, and f) show that Hf, Zr, Nb, Ta, and Co are broadly distributed throughout the agglomerated powder particles. Irregular regions with weak or absent EDS signals were observed. These regions are attributed primarily to signal attenuation associated with the three-dimensional surface topography and particle overlap within the agglomerates, rather than necessarily indicating porous or regions devoid of the constituent elements. Localized Co-enriched spots are also observed at the submicron scale. However, given the spatial resolution and the complex morphology of the agglomerated powders, these EDS features alone cannot conclusively distinguish local compositional fluctuations from discrete Co-containing nanoparticles or phases.

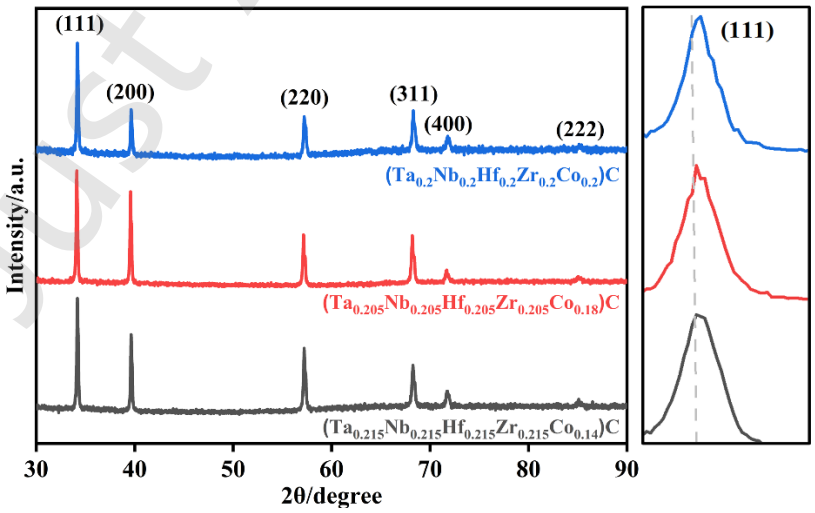


Figure 1 XRD patterns of $(Hf_{(1-X)/4}Zr_{(1-X)/4}Nb_{(1-X)/4}Ta_{(1-X)/4}Co_X)C$ (X = 0.14, 0.18, and 0.20) powders synthesized at 1900°C, showing the formation of a single-phase FCC structure

Just Accepted

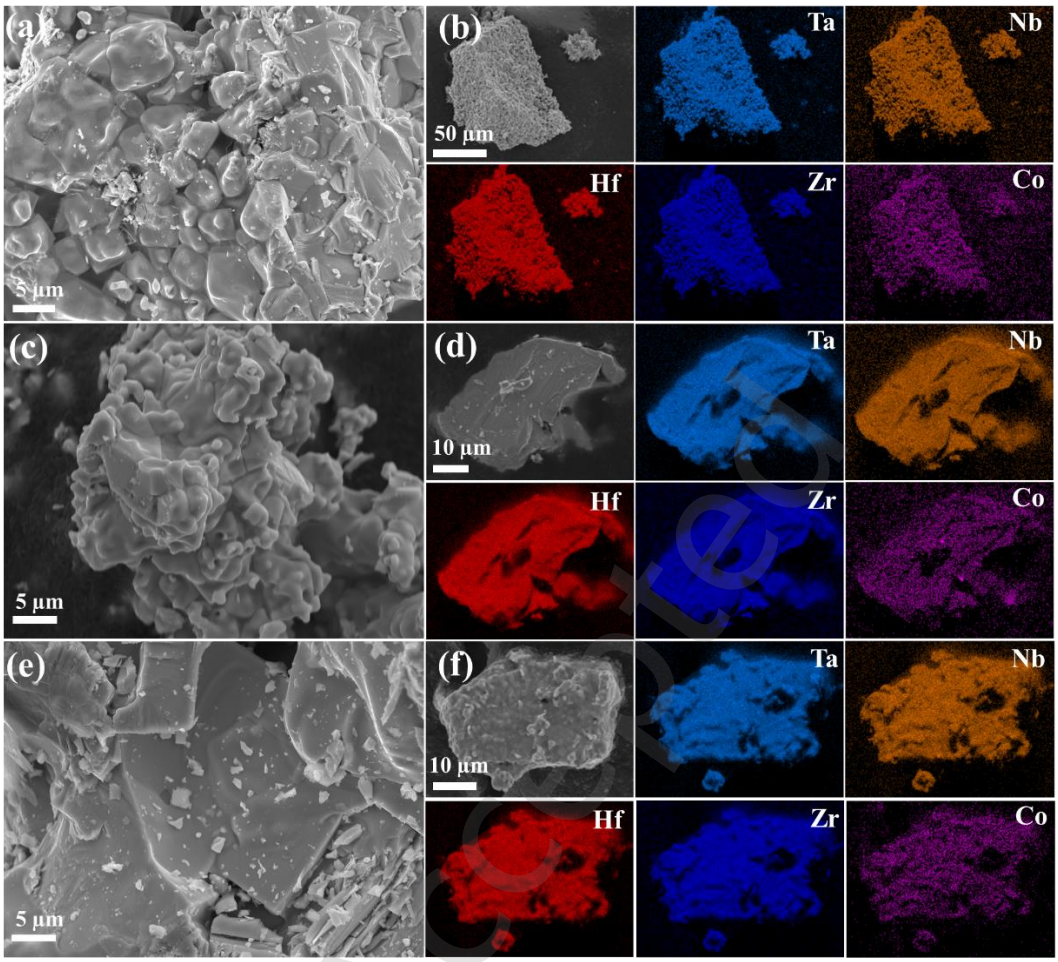


Figure 2 SEM images and corresponding EDS elemental mappings of $(Hf_{(1-X)/4}Zr_{(1-X)/4}Nb_{(1-X)/4}Ta_{(1-X)/4}Co_X)C$ (X = 0.14, 0.18, and 0.20) powders: (a, b) $(Hf_{0.215}Zr_{0.215}Nb_{0.215}Ta_{0.215}Co_{0.140})C$; (c, d) $(Hf_{0.205}Zr_{0.205}Nb_{0.205}Ta_{0.205}Co_{0.180})C$; (e, f) $(Hf_{0.20}Zr_{0.20}Nb_{0.20}Ta_{0.20}Co_{0.20})C$. (a, c, e) SEM images; (b, d, f) EDS elemental mappings of Hf, Zr, Nb, Ta, and Co.

3.2 Phase and microstructure of the HEC bulk samples

Figure 3 presents the XRD patterns of the HEC1, HEC2, and HEC3 bulk samples sintered at 1900 °C under a pressure of 6 GPa. All diffraction peaks can be indexed to the FCC carbide phase, with no detectable secondary-phase diffraction peaks. This indicates that the FCC carbide remains the dominant crystalline phase, although the

Just Accepted

absence of detectable secondary-phase peaks does not necessarily exclude the presence of a minor secondary phase. The lattice parameters of HEC1, HEC2, and HEC3, calculated from the XRD data, are 4.5494 Å, 4.5543 Å, and 4.5498 Å, respectively. To further examine the structural characteristics, first-principles calculations were performed, yielding a lattice constant of 4.4500 Å for $(Hf_{0.2}Zr_{0.2}Nb_{0.2}Ta_{0.2}Co_{0.2})C$, which is slightly smaller than the experimental values. This discrepancy may be attributed to differences between theoretical calculations at 0 K and experimental measurements at finite temperatures, as well as thermal expansion and residual lattice distortion.

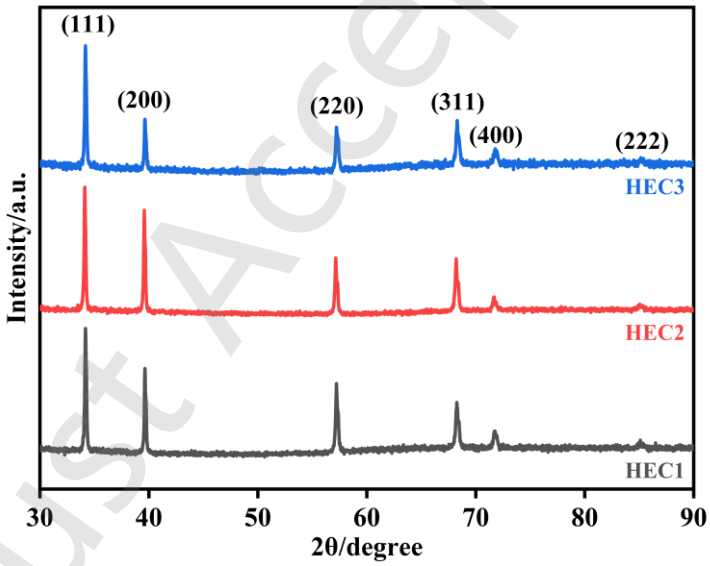


Figure 3 XRD patterns of HEC1, HEC2, and HEC3 bulk samples sintered at 1900 °C under a pressure of 6 GPa, showing the formation of a single-phase FCC structure.

Figure 4 presents the SEM images of HEC1, HEC2, and HEC3, respectively. All bulk samples exhibit a high degree of densification under the combined effects of elevated temperature and high pressure. Nevertheless, irregular and rugged surface morphologies are observed, which can be attributed to heterogeneous plastic flow,

Just Accepted

localized densification variations, and the sluggish diffusion characteristics inherent to high-entropy ceramics during high-pressure sintering of bulk samples. Figures 4c, f, and i present the corresponding EDS elemental distribution maps. While Hf, Zr, Nb, and Ta elements are homogeneously distributed, the Co element exhibits noticeable segregation and localized enrichment in all samples. These Co-rich regions are also discernible in the SEM images, suggesting the occurrence of partial phase separation during sintering. Figure 5 presents the EBSD analysis of HEC1, HEC2, and HEC3. The inverse pole figure (IPF) maps (Figures 5a–c) show no pronounced preferred crystallographic orientation in the examined regions, suggesting that strong crystallographic texture is unlikely to be a dominant factor in the observed differences in mechanical properties. The corresponding phase maps (Figures 5d–f) confirm that the matrix retains a dominant single-phase structure, while the segregated Co is primarily distributed along grain boundaries. No clear dependence of grain size on Co content is observed. The fraction of low-angle grain boundaries in bulk samples (LAGBs, 2–15°) increases from 20.2% in HEC1 to 25.0% in HEC2 and further to 37.9% in HEC3.

Just Accepted

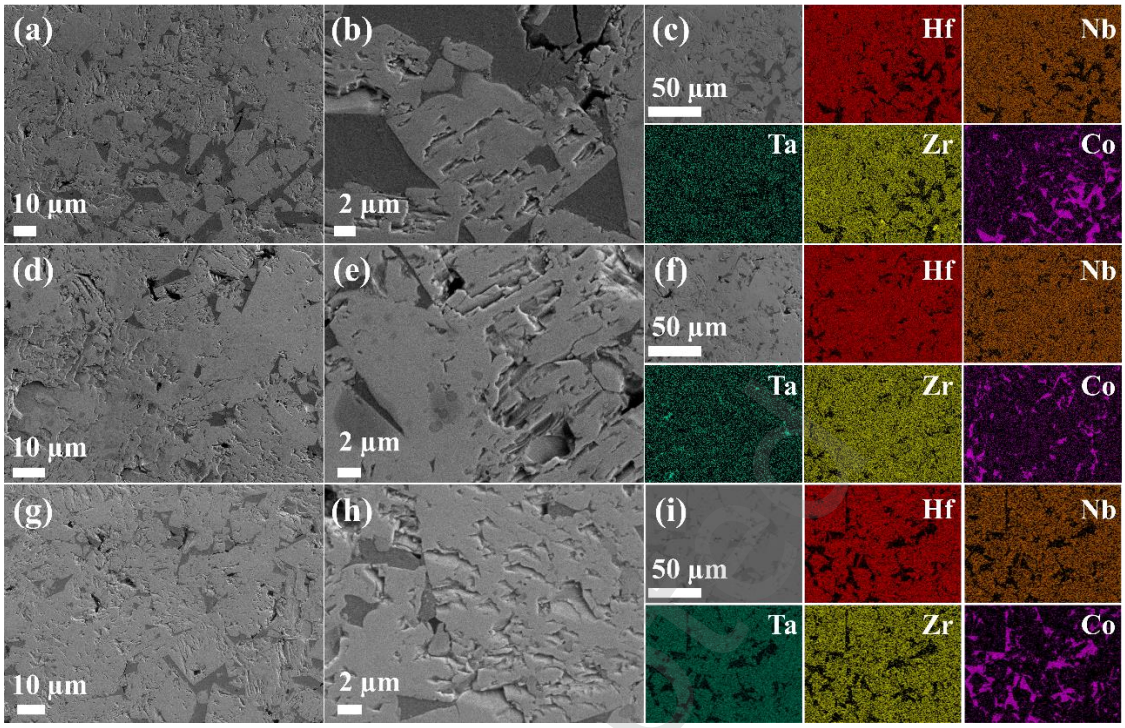


Figure 4 SEM images, EDS elemental mapping, and particle size distributions of HEC1, HEC2, and HEC3 bulk samples: (a, d, g) lower-resolution SEM images; (b, e, h) high-resolution SEM images; (c, f, i) EDS maps showing the distribution of Hf, Zr, Nb, Ta, and Co.

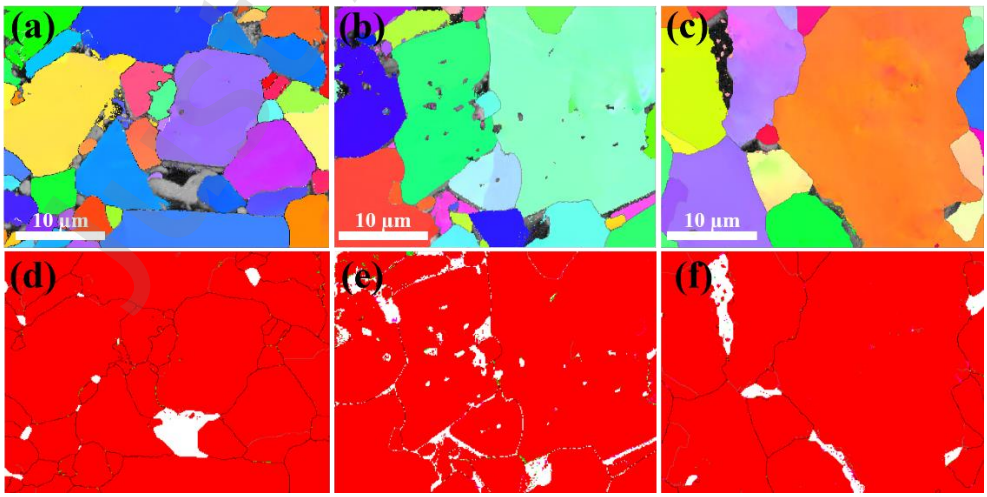


Figure 5 EBSD results of HEC1, HEC2, and HEC3 bulk samples: (a–c) IPF maps showing randomly oriented grains; (d–f) phase maps indicating a dominant single-phase matrix with Co segregation primarily located at grain boundaries.

Figure 6 displays transmission electron microscopy (TEM) characterization of the interface between the HEC and precipitated Co phase in HEC3. Figure 6a presents the overview TEM image, where distinct phase contrast can be observed. Figure 6b shows a high-resolution TEM (HRTEM) image of region A in Figure 6a, revealing two adjacent grains separated by a well-defined interface, with a thin transition layer clearly visible. Figure 6c presents the fast Fourier transform (FFT) image and its corresponding inverse fast Fourier transform (IFFT) image of grain B in Figure 6b. The measured interplanar spacing of 0.2335 nm corresponds to the (200) plane of the HEC phase, consistent with the XRD results. Figure 6d presents the FFT and IFFT results from the grain boundary region (region C). Compared with Figure 6c, additional diffraction spots are observed, which can be attributed to the presence of the precipitated Co phase. The measured interplanar spacing is 0.1122 nm, corresponding to the (220) plane of the cubic Co phase. The IFFT image further reveals a high-density distribution of dislocations near the interface. Figure 6e shows the selected area electron diffraction (SAED) pattern of the HEC matrix, exhibiting a typical FCC diffraction pattern with a zone axis along the [-100] direction. Figure 6f presents the SAED pattern of the Co-rich region, which also displays an FCC structure with a zone axis along the [112] direction. As shown in Figure 6g, the EDS elemental mapping at the grain boundary reveals slight segregation of Nb and Zr within the transition layer. This behavior is associated with their relatively lower meta-carbon bonding strength and higher sensitivity to local lattice distortion, which promotes elemental redistribution at the interface [47].

Just Accepted

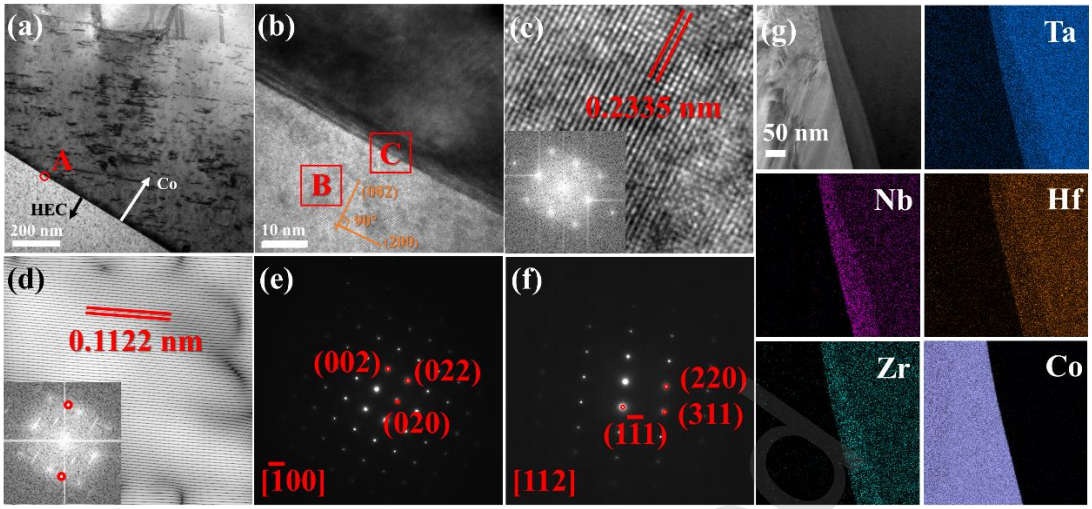


Figure 6 TEM characterization of HEC3: (a) overview image; (b) high-resolution TEM (HRTEM) image at the grain boundary (region A); (c) Fast Fourier Transform (FFT) and inverse FFT (IFFT) of region B in (b); (d) FFT and IFFT of region C in (b); (e) selected area electron diffraction (SAED) pattern of the HEC matrix in (a); (f) SAED pattern of the Co-rich region in (a); (g) EDS elemental mapping at the interface.

3.3 Mechanical properties of the HEC bulk samples

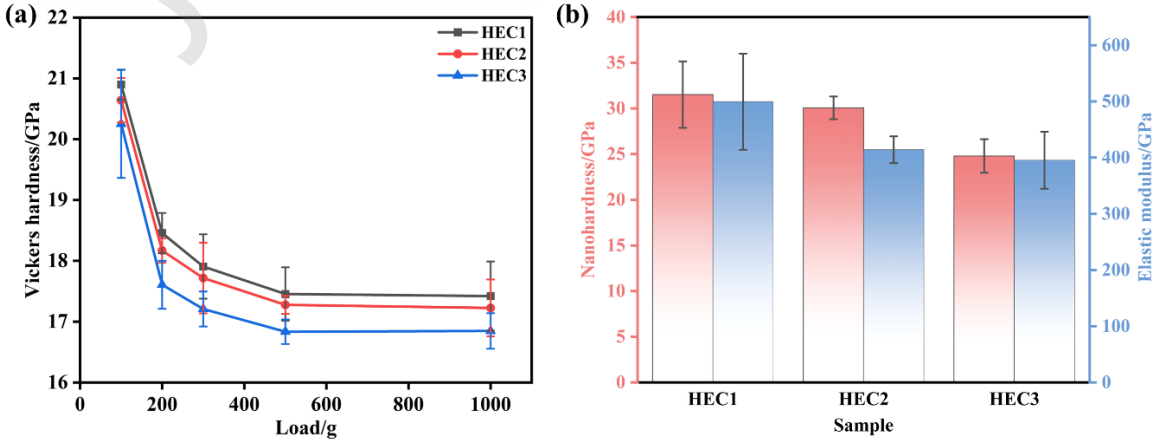
Vickers hardness measurements were conducted on HEC1, HEC2, and HEC3. As shown in Figure 7a, all samples exhibit a typical indentation size effect, where hardness decreases with increasing load and gradually approaches a plateau. The equilibrium Vickers hardness values are 17.42 GPa for HEC1, 17.23 GPa for HEC2, and 16.85 GPa for HEC3, indicating a slight decrease in hardness with increasing Co content. Figure 7b presents the nanoindentation results. The nanohardness and elastic modulus of HEC1 are 31.52 GPa and 499.60 GPa, respectively; those of HEC2 are 30.06 GPa and 414.17 GPa; and those of HEC3 are 24.79 GPa and 395.39 GPa. The fracture toughness values, calculated using Equation (1), are 4.54 MPa·m$^{1/2}$ for HEC1, 4.72 MPa·m$^{1/2}$ for HEC2, and 4.98 MPa·m$^{1/2}$ for HEC3. In contrast to hardness and modulus, fracture

Just Accepted

toughness shows a continuous increase with increasing Co content. Table 1 compares the mechanical properties of the present HEC samples with those of representative binary carbides and previously reported high-entropy carbides. These results demonstrate that HEC1–HEC3 achieve a favorable balance between hardness and toughness, exhibiting competitive toughness while maintaining relatively high hardness among advanced carbide systems.

Table 1 Comparison of mechanical properties of the present HEC bulk samples with previously reported high-entropy carbides synthesized via different routes.

Samples	Vickers hardness/GPa	Nano hardness/GPa	Elastic modulus/Gpa	Fracture toughness/ MPa·m$^{1/2}$	Reference
HEC1	17.4 ± 0.6	31.5 ± 3.6	499.6 ± 85.6	4.5 ± 0.2	This work
HEC2	17.2 ± 0.5	30.1 ± 1.2	414.2 ± 23.8	4.7 ± 0.2	This work
HEC3	16.8 ± 0.3	24.8 ± 1.8	395.4 ± 50.9	5.0 ± 0.2	This work
$(Hf_{0.2}Zr_{0.2}Ti_{0.2}Ta_{0.2}Nb_{0.2})C$	25.0 ± 1.0	-	450	3.5 ± 0.3	[48]
$(Ti_{0.2}Cr_{0.2}Nb_{0.2}Ta_{0.2}V_{0.2})C$	24.6 ± 0.8	36.6 ± 0.5	476 ± 13	2.4 ± 0.3	[49]
$(Hf_{0.2}Mo_{0.2}Nb_{0.2}Ta_{0.2}Ti_{0.2})C$	18.5	-	-	4.2	[50]
$(Ti_{0.25}Zr_{0.25}Nb_{0.25}Ta_{0.25})C$	21.82 ± 1.5	-	-	4.565 ± 0.5	[51]
(NbTaZrTiHfVWMo)C	-	38.71	-	4.67	[52]
$(Ti_{0.2}Zr_{0.2}Hf_{0.2}V_{0.2}Nb_{0.2})C$	24.3	-	429.1	3.4	[53]



Just Accepted

Figure 7 Mechanical properties of HEC bulk samples: (a) Vickers hardness as a function of applied load, showing a typical indentation size effect; (b) nanoindentation results, including nanohardness and elastic modulus.

3.4 Phase Stability and Decomposition of Co-Containing HEC

To investigate the thermodynamic tendency for Co segregation, a possible decomposition pathway was considered, in which the Co-containing HEC decomposes into a Co-free quaternary carbide and elemental Co:

$$(Hf_{0.2}Zr_{0.2}Nb_{0.2}Ta_{0.2}Co_{0.2})C_{1-x} \rightarrow (Hf_{0.25}Zr_{0.25}Nb_{0.25}Ta_{0.25})C_{1-y} + Co + C \quad (2)$$

In this reaction, the initial Co-containing HEC and the residual quaternary carbide are represented by $(Hf_{0.2}Zr_{0.2}Nb_{0.2}Ta_{0.2}Co_{0.2})C_{1-x}$ and $(Hf_{0.25}Zr_{0.25}Nb_{0.25}Ta_{0.25})C_{1-y}$, respectively, to account for possible carbon vacancies in both carbide phases. Accordingly, the reaction does not explicitly assume the formation of a fixed amount of excess free carbon. The values of x and y cannot be experimentally established, and Equation (2) represents a proposed decomposition pathway rather than a quantitative description of the actual phase compositions or carbon balance in the sintered samples.

For the first-principles calculations, an idealized stoichiometric rock-salt model was adopted, in which Co occupies the transition-metal sublattice. Specifically, the calculations correspond to the limiting case of $x = y = 0$, assuming complete Co segregation and the formation of a stoichiometric Co-free quaternary carbide. Thus, the calculated reaction energies are used to evaluate the thermodynamic tendency for Co segregation within this idealized model, rather than to quantitatively predict the phase compositions or fractions in the experimental samples.

Just Accepted

Within the static 0 K DFT framework, the Gibbs free-energy change was approximated as:

$$\Delta G \approx \Delta H = \Delta E + \mathrm{P} \cdot \Delta \mathrm{V} \quad (3)$$

As summarized in Table 2, with the underlying computational data provided in Table S1 and Table S2, the calculated (ΔG) remains negative over 0–6 GPa and becomes more negative with increasing pressure. This result indicates that the considered decomposition pathway becomes thermodynamically more favorable under pressure within the adopted model.

Table 2 DFT-calculated formation energies of the corresponding reaction energy change ΔE and the resulting ΔV and ΔG of the decomposition reaction.

P/GPa	ΔE/eV	ΔV/Å^3	ΔG/eV
0	-78.06	-72.999	-78.06
2	-78.03	-71.835	-78.92
3	-78.03	-71.312	-79.37
4	-78.00	-71.288	-79.78
5	-77.97	-70.780	-80.18
6	-77.94	-70.282	-80.57

The electronic origin of the predicted Co instability was examined using COHP, DOS, and charge-density analyses (Figures S2–S10). Co–C exhibits pronounced antibonding states near the Fermi level, whereas Hf–C, Zr–C, Nb–C, and Ta–C exhibit more favorable bonding characteristics. This contrast suggests that Co–C interactions provide less stabilization than the refractory transition-metal-C (TM-C) bonding network. These pressure-dependent ICOHP values further reveal an increasing bonding asymmetry (Figure 8a). From 0 to 6 GPa, the ICOHP values of Hf–C, Zr–C, Nb–C, and Ta–C change from −2.18 to −2.24 eV, −1.79 to −1.86 eV, −2.00 to −2.17 eV, and −2.24

Just Accepted

to −2.33 eV, respectively, indicating stronger bonding interactions. In contrast, the Co–C ICOHP changes from −2.06 to −2.03 eV, indicating a slight weakening of Co–C bonding, providing a slight weakening of Co-C interactions. These results suggest that pressure preferentially strengthens the TM–C framework relative to Co–C bonding, providing an electronic-structure explanation consistent with the predicted tendency for Co segregation.

The associated local structural response was examined using Voronoi and Bader volume analyses, together with the Co–Co radial distribution function (RDF) (Figures 8b and S11). The reduction in the Voronoi and Bader volumes associated with Co is consistent with local compression under pressure. Meanwhile, the first Co–Co RDF peak increases in intensity from 15.97 to 24.50 and shifts from approximately 3.14 to 3.10 Å between 0 and 6 GPa, indicating enhanced short-range Co–Co correlations and reduced Co–Co separation. Collectively, these results suggest that pressure-induced bonding asymmetry promotes local structural rearrangement and Co–Co association, consistent with the experimentally observed Co-rich regions.

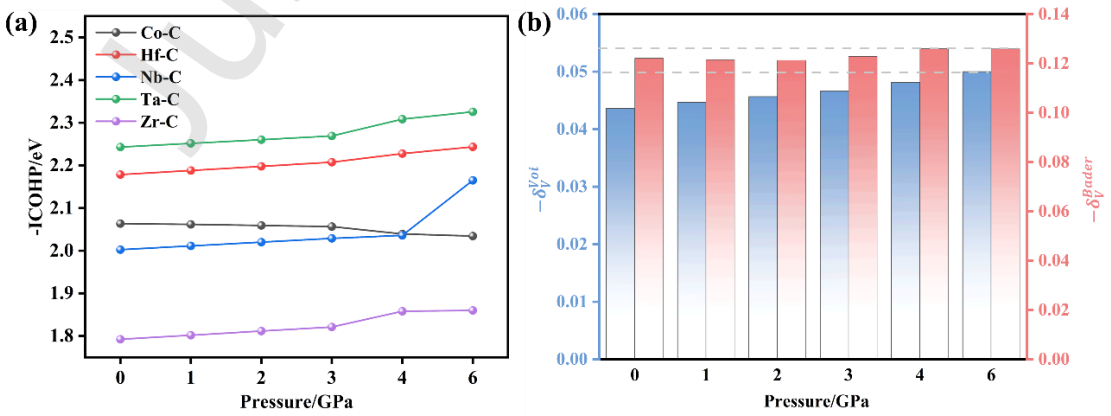


Figure 8 (a) ICOHP values for metal–carbon bonds, reflecting bond strength; (b) atomic volume misfit and Bader volume misfit of Co atoms under different pressures.

Just Accepted

3.5 Toughening Mechanisms Induced by Co Precipitation

Figure 9a shows a representative TEM image of HEC3. It reveals the microstructural features associated with Co precipitation. The HRTEM image in Figure 9b (region A in Figure 9a) shows a distinct Co-rich region. A FFT analysis of region C confirmed that it corresponds to single-phase Co. Notably, a high density of dislocations was observed within the Co region, indicating not only strong plastic deformation capacity but also directly promoting the formation of subgrains, thereby providing a fundamental explanation for the increase in the LAGB ratio with increasing Co content. The IFFT image in Figure 9c further reveals that these defects are predominantly edge dislocations, which play a critical role in strain accommodation. Figure 9d shows the HRTEM image of the interface region (region B in Figure 9a). The measured interplanar spacings are 0.2252 nm for FCC-Co and 0.2618 nm for the HEC matrix, indicating an inherent lattice mismatch. However, the geometric phase analysis (GPA) result in Figure 9e shows a relatively uniform and low strain distribution at the interface. This suggests that the lattice mismatch is effectively relaxed, despite the structural discontinuity. The SAED pattern in Figure 9f exhibits two independent sets of diffraction spots, confirming that the Co precipitates and HEC matrix have the relation of [312] HEC∥[101] Co. Meanwhile, the EDS mapping in Figure 9g shows a distinct Co-enriched interfacial region with disordered atomic stacking. These observations collectively indicate the formation of a structurally discontinuous yet mechanically compatible interface. The apparent contradiction between structural discontinuity and low interfacial strain can be rationalized by the intrinsic properties of the Co phase. The

Just Accepted

FCC Co phase, enriched at the interface, provides substantial plasticity and enables local atomic rearrangement. In addition, the high density of dislocations within the Co phase facilitates strain relaxation, leading to the formation of a quasi-stress-free interface. This ductile interfacial layer effectively accommodates lattice mismatch and reduces stress concentration.

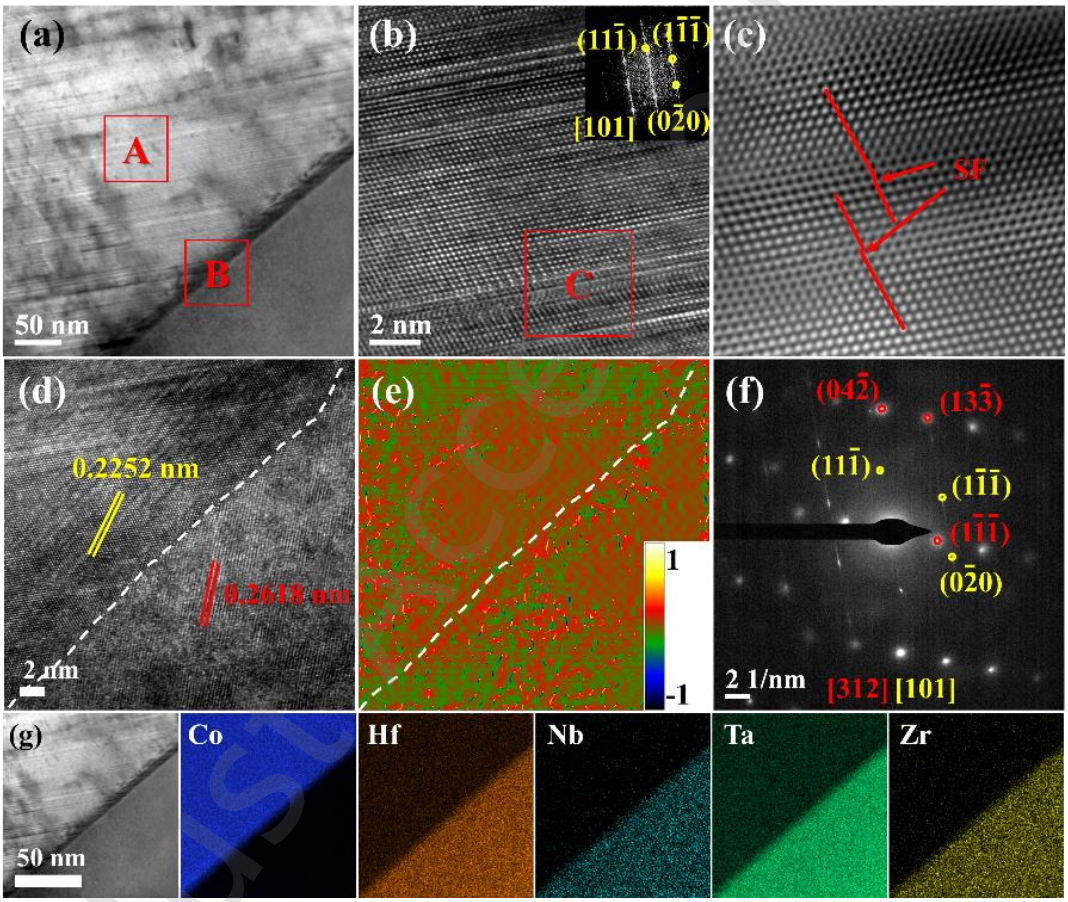


Figure 9 TEM characterization of HEC3: (a) overall microstructure; (b) HRTEM image of region A with corresponding FFT of region C; (c) IFFT image showing dislocation structures; (d) HRTEM image of the interface (region B); (e) GPA strain map of (d); (f) SAED pattern at the interface; (g) EDS elemental mapping across the interface.

Figure 10a shows the indentation morphology of HEC3 under a load of 500 g. High-magnification images (Figure 10b–d) reveal that cracks exhibit pronounced

branching and deflection during propagation. No significant crystallographic texture was observed between HEC1 and HEC3, indicating that the differences in mechanical properties are unlikely to result from texture evolution. The increased fraction of LAGBs and the high density of dislocations near interfaces further contribute to plastic deformation at the microscale. These features facilitate crack deflection, crack bridging, and crack tip blunting during fracture, thereby enhancing energy dissipation and suppressing crack propagation. More importantly, the precipitated Co acts as a compliant buffer during crack propagation. Instead of fracturing, the Co phase undergoes plastic deformation, absorbing fracture energy and promoting crack deflection or re-initiation at adjacent interfaces. This behavior introduces an additional energy dissipation mechanism and interrupts straight crack propagation paths. Furthermore, the presence of crack branching and transgranular fracture indicates strong grain boundary cohesion in the HEC matrix. As a result, cracks are forced to propagate through grains, accompanied by frequent deflection and path deviation, which further increases the fracture resistance [54–56].

Just Accepted

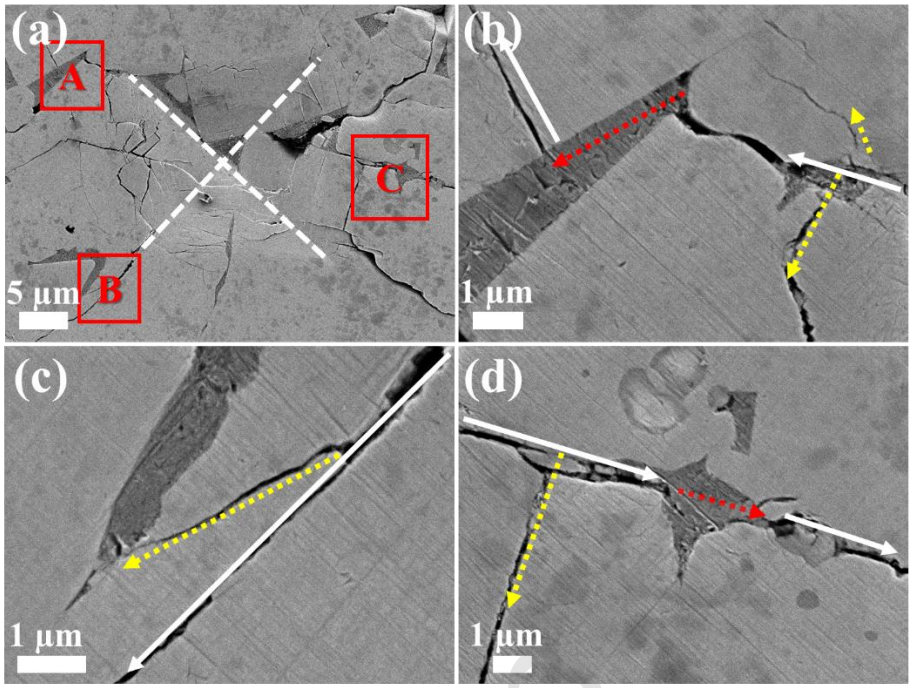


Figure 10 SEM images of indentation morphology of HEC3 under a 500 g load: (a) overall view; (b–d) high-magnification images of regions A, B, and C in (a)

4. Conclusions

This work uncovers a fundamental mechanism by which electronic-structure instability governs phase separation and toughening in Co-containing high-entropy carbides. The key findings are summarized as follows:

(1) First-principles calculations reveal that Co incorporation introduces antibonding Co–C states near the Fermi level, in contrast to the stable TM–C covalent framework. This intrinsic electronic instability renders the solid solution thermodynamically unfavorable, as evidenced by the negative decomposition Gibbs free energy across the investigated pressure range.

(2) External pressure enhances bonding asymmetry, further destabilizing Co–C interactions and promoting phase separation. This process is accompanied by

Just Accepted

pronounced local lattice distortion, atomic volume mismatch, and Co clustering, establishing a direct link between electronic structure and short-range atomic ordering.

(3) The segregated Co forms a ductile FCC phase along grain boundaries, enabling strain accommodation through dislocation activity. Despite structural discontinuity, these interfaces remain mechanically compatible, effectively suppressing stress concentration.

(4) The Co-rich interfacial phase promotes crack deflection, branching, and energy dissipation, leading to enhanced fracture resistance. Toughening thus arises from an electronically driven microstructural transformation rather than external reinforcement.

(5) These findings establish a paradigm in which controlled electronic instability is leveraged to induce beneficial phase separation, offering a broadly applicable strategy for designing damage-tolerant high-entropy ceramics.

Just Accepted

Declaration of competing interest

The author declare that they have no known competing financial interests or personal relationships that could have appeared to influence the work reported in this paper.

Just Accepted

Acknowledgements

This work was supported by Guangzhou Municipal Basic Research Program – Jointly Funded by Municipal Government, Universities, Research Institutes and Enterprises (SL2024A03J00679), National Natural Science Foundation of China (52272058, 52302063), Young Elite Scientist Sponsorship Program by CAST (2023QNRC001), and Innovation Training Program for Postgraduates of Guangzhou University (JCCX2025054).

Just Accepted

References

[1] Hingangavkar GM. High-entropy ceramics: From disorder to emerging functionalities. *Ceram Int* 2025, **51**: 63519–36.

[2] Li Y, Pan D, Cao J, *et al.* Recent advances in high-entropy ceramics: Design principles, structural characteristics, and emerging properties. *Ext Mater* 2025, **1**: 42–72.

[3] Xiang H, Xing Y, Dai F zhi, *et al.* High-entropy ceramics: Present status, challenges, and a look forward. *J Adv Ceram* 2021, **10**: 385–441.

[4] Dippo OF, Vecchio KS. A universal configurational entropy metric for high-entropy materials. *Scr Mater* 2021, **201**: 113974.

[5] Wu J, Zhang J, Hu X, *et al.* Ultrahigh degree of cationic disorder, configurational entropy in new type of high-entropy pseudobrookite phase. *Small* 2024, **20**: 2310615.

[6] Liu J, Shao G, Liu D, *et al.* Design and synthesis of chemically complex ceramics from the perspective of entropy. *Mater Today Adv* 2020, **8**: 100114.

[7] Akrami S, Edalati P, Fuji M, *et al.* High-entropy ceramics: Review of principles, production and applications. *Mater Sci Eng R Rep* 2021, **146**: 100644.

[8] Zhou J, Zhang J, Zhang F, *et al.* High-entropy carbide: A novel class of multicomponent ceramics. *Ceram Int* 2018, **44**: 22014–8.

[9] Ni D, Cheng Y, Zhang J, *et al.* Advances in ultra-high temperature ceramics, composites, and coatings. *J Adv Ceram* 2022, **11**: 1–56.

[10] Harrington TJ, Gild J, Sarker P, *et al.* Phase stability and mechanical properties of

Just Accepted

novel high entropy transition metal carbides. *Acta Mater* 2019, **166**: 271–80.

[11] Liu SY, Zhang S, Liu S, *et al.* Stability and mechanical properties of single-phase quinary high-entropy metal carbides: First-principles theory and thermodynamics. *J Eur Ceram Soc* 2022, **42**: 3089–98.

[12] Esters M, Oses C, Hicks D, *et al.* Settling the matter of the role of vibrations in the stability of high-entropy carbides. *Nat Commun* 2021, **12**: 5747.

[13] Shao Z, Zeng D, Xu M, *et al.* A novel highly porous dual-phase high-entropy ultrahigh-temperature ceramic with outstanding properties. *J Adv Ceram* 2025, **14**: 9221132.

[14] Biesuz M, Saunders TG, Veverka J, *et al.* Solidification microstructures of multielement carbides in the high entropy Zr-Nb-Hf-Ta-Cx system produced by arc melting. *Scr. Mater.* 2021, **203**: 114091.

[15] Kong Q, Zhang R, Chen L, *et al.* Phase transition of multi-component (TiZrVNb)C ceramics— part I: Phase decomposition induced by carbon content. *J Adv Ceram* 2024, **13**: 679–88.

[16] Zhang W, Li K, Chen L, *et al.* The phase decomposition in non-equimolar (ZrHfVNbMoW)Cx complex concentrated carbides via carbon content regulation. *J Eur Ceram Soc* 2024, **44**: 1396–403.

[17] Luo SC, Guo WM, Plucknett K, *et al.* Low-temperature densification of high-entropy (Ti,Zr,Nb,Ta,Mo)C—Co composites with high hardness and high toughness. *J Adv Ceram* 2022, **11**: 805–13.

[18] Liu Y, Liang J, Guo W, *et al.* Cr-assisted low-temperature densification of

Just Accepted

(Ti,Zr,Nb,Ta,Mo)C high-entropy carbides with ultrafine grain and enhanced hardness. *J Adv Ceram* 2024, **13**: 780–8.

[19] Zhao B, Wang D, Qi G, *et al.* Enhancing hardness-toughness synergy through entropy gain effects: Implications for ceramic cutting tool materials. *J Alloy Compd* 2024, **1005**: 176131.

[20] Cao Z, Sun J, Meng L, *et al.* Progress in densification and toughening of high entropy carbide ceramics. *J Mater Sci Technol* 2023, **161**: 10–43.

[21] Zhang R, Wang S, Zheng L, *et al.* Bamboo-inspired fibrous monolithic high-entropy carbide ceramics with enhanced toughness and thermal insulation performance. *J Adv Ceram* 2025, **14**: 9221190.

[22] Habibnia D, Balak Z. A novel (HfTaZrTiV) C high-entropy ceramic with submicron grains: Role of graphite and si additives. *JOM* 2026, **78**: 6844–57.

[23] Malae Hezarvandi S, Balak Z, Heiydary Moghadam A. Fabrication and characterization of HfCZrCTiC composites: Role of carbonaceous and metallic additives. *J Korean Ceram Soc* 2024, **61**: 1263–77.

[24] Peng F, Wei Z, Song Q, *et al.* Simultaneous hardening and toughening of a high-entropy (NbTaZrW)C ceramic carbide using SiC particle. *J Am Ceram Soc* 2023, **106**: 4443–54.

[25] Li H, Yang Z, Lian M, *et al.* Enhanced toughness of high-entropy $(Ti_{0.2}Zr_{0.2}Hf_{0.2}Nb_{0.2}Ta_{0.2})C$ ceramics with SiC whiskers by high-pressure and high-temperature sintering. *Materials* 2025, **18**: 1655.

[26] Li YT, Chen XM, Zeng XK, *et al.* Hard yet tough and self-lubricating

Just Accepted

(CuNiTiNbCr)C high-entropy nanocomposite films: Effects of carbon content on structure and properties. *J Mater Sci Technol* 2024, **173**: 20–30.

[27] Sun J, Zhao J, Zhou Y, *et al.* High-performance multifunctional ($Hf_{0.2}$ $Nb_{0.2}$ $Ta_{0.2}$ $Ti_{0.2}$ $Zr_{0.2}$)C high-entropy ceramic reinforced with low-loading 3D hybrid graphene–carbon nanotube. *J Adv Ceram* 2023, **12**: 341–56.

[28] Sun J, Zhao J, Chen Y, *et al.* Toughening in low-dimensional nanomaterials high-entropy ceramic nanocomposite. *Compos Part B Eng* 2022, **231**: 109586.

[29] Cai K, Sun J, Li X, *et al.* Crack propagation and mechanical behavior prediction of graphene reinforced functionally gradient high-entropy cemented carbides. *Mater Today Commun* 2024, **41**: 110861.

[30] Guan S, Liang H, Wang Q, *et al.* Synthesis and phase stability of the high-entropy carbide ($Ti_{0.2}$ $Zr_{0.2}$ $Nb_{0.2}$ $Ta_{0.2}$ $Mo_{0.2}$)C under extreme conditions. *Inorg Chem* 2021, **60**: 3807–13.

[31] Guan S, Lin W, Liang H, *et al.* The effect of pressure tuning on the structure and mechanical properties of high-entropy carbides. *Scr Mater* 2022, **216**: 114755.

[32] Wang Y. Processing and properties of high entropy carbides. *Adv Appl Ceram* 2022, **121**: 57–78.

[33] Bini R, Ceppatelli M, Citroni M, *et al.* From simple to complex and backwards. Chemical reactions under very high pressure. *Chem Phys* 2012, **398**: 262–8.

[34] Zhang L, Wang Y, Lv J, *et al.* Materials discovery at high pressures. *Nat Rev Mater* 2017, **2**: 17005.

[35] Grochala W, Hoffmann R, Feng J, *et al.* The chemical imagination at work in *very*

Just Accepted

tight places. *Angew Chem Int Ed* 2007, **46**: 3620–42.

[36] Quesne MG, Roldan A, De Leeuw NH, *et al.* Bulk and surface properties of metal carbides: Implications for catalysis. *Phys Chem Chem Phys* 2018, **20**: 6905–16.

[37] Råsander M, Lewin E, Wilhelmsson O, *et al.* Carbon release by selective alloying of transition metal carbides. *J Phys Condens Matter* 2011, **23**: 355401.

[38] Häglund J, Fernández Guillermet A, Grimvall G, *et al.* Theory of bonding in transition-metal carbides and nitrides. *Phys Rev B* 1993, **48**: 11685–91.

[39] Wijeyesekera SD, Hoffmann R. Transition metal carbides. A comparison of bonding in extended and molecular interstitial carbides. *Organometallics* 1984, **3**: 949–61.

[40] Weinberger CR, Thompson GB. Review of phase stability in the group IVB and VB transition-metal carbides. *J Am Ceram Soc* 2018, **101**: 4401–24.

[41] Kresse G, Furthmüller J. Efficiency of ab-initio total energy calculations for metals and semiconductors using a plane-wave basis set. *Comp Mater Sci* 1996, **6**: 15–50.

[42] Kresse G, Furthmüller J. Efficient iterative schemes for *ab initio* total-energy calculations using a plane-wave basis set. *Phys Rev B* 1996, **54**: 11169–86.

[43] Van De Walle A, Tiwary P, De Jong M, *et al.* Efficient stochastic generation of special quasirandom structures. *Calphad* 2013, **42**: 13–8.

[44] Perdew JP, Burke K, Ernzerhof M. Generalized gradient approximation made simple. *Phys Rev Lett* 1996, **77**: 3865–8.

[45] Wang S, Ouyang Y, Guo L, *et al.* Boosting microwave attenuation in high-entropy

Just Accepted

carbide ceramics via magnetic co incorporation and microstructural engineering. *J Adv Ceram* 2025.

[46] Guo Y, Staedler T, Müller J, *et al.* A detailed analysis of the determination of fracture toughness by nanoindentation induced radial cracks. *J Eur Ceram Soc* 2020, **40**: 276–89.

[47] Dai FZ, Wen B, Sun Y, *et al.* Grain boundary segregation induced strong UHTCs at elevated temperatures: A universal mechanism from conventional UHTCs to high entropy UHTCs. *J Mater Sci Technol* 2022, **123**: 26–33.

[48] Feng L, Chen W, Fahrenholtz WG, *et al.* Strength of single-phase high-entropy carbide ceramics up to 2300°C. *J Am Ceram Soc* 2021, **104**: 419–27.

[49] Mao H, Dong E, Jin S, *et al.* Ultrafast high-temperature synthesis and densification of high-entropy carbides. *J Eur Ceram Soc* 2022, **42**: 4053–65.

[50] Sun Q, Tan H, Zhu S, *et al.* Single-phase (Hf-Mo-Nb-Ta-Ti)C high-entropy ceramic: A potential high temperature anti-wear material. *Tribol Int* 2021, **157**: 106883.

[51] Cao D, Yu M, Dong Q, *et al.* Metal-organic-gel method derived (TiZrNbTa)C high-entropy nanopowders and ceramics with high performance. *Ceram Int* 2025, **51**: 38599–608.

[52] He L, Liu L, Peng F, *et al.* Host lattice and solid solution formation in an octal-cation (NbTaZrTiHfVWMo)C high entropy carbide ceramic. *J Eur Ceram Soc* 2023, **43**: 5792–801.

[53] Wang Z, Liu G, Gao W, *et al.* Mechanical behavior of high entropy ceramic $(TiZrHfVNb)C_5$ under extreme conditions: A first-principles density functional

Just Accepted

theory study. *Ceram Int* 2024.

[54] Al-Habib DSH, Balak Z, Asl MS. Spark plasma sinterability of TaC-based composites co-doped with SiC, TiC and graphene. *Diam Relat Mater* 2022, **130**: 109496.

[55] Savari V, Balak Z, Shahedifar V. Combined and alone addition effect of nano carbon black and SiC on the densification and fracture toughness of SPS-sintered ZrB2. *Diam Relat Mater* 2022, **128**: 109244.

[56] Savari V, Balak Z, Shahedifar V. Influence of graphite platelets with and without SiC on the densification and fracture toughness of ZrB_2 ceramic sintered by SPS. *Carbon Lett* 2022, **32**: 1559–66.

Just Accepted